J. Fluid Mech. (2011), *vol.* 676, *pp.* 81–109. © Cambridge University Press 2011
doi:10.1017/jfm.2011.34

Control of laminar separation using pulsed vortex generator jets: direct numerical simulations

D. POSTL, W. BALZER AND H. F. FASEL†

Department of Aerospace and Mechanical Engineering, University of Arizona, Tucson, AZ 85721, USA

(Received 24 May 2010; revised 17 December 2010; accepted 17 January 2011;
first published online 19 April 2011)

Direct numerical simulations (DNS) are employed to investigate laminar boundary layer separation and its control by pulsed vortex generator jets (VGJs), i.e. by injecting fluid into the flow through a spanwise array of small holes. Particular focus is directed towards identifying the relevant physical mechanisms associated with VGJ control of low-Reynolds-number separation, as encountered in low-pressure turbine applications. Pulsed VGJs are shown to be much more effective than steady VGJs when the same momentum coefficient is used for the actuation. From our investigations we have found that the increased control effectiveness of pulsed VGJs can be explained by the fact that linear hydrodynamic instability mechanisms are exploited. When pulsing with frequencies to which the separated shear layer is naturally unstable, instability modes are shown to develop into large-scale, spanwise coherent structures. These structures provide the necessary entrainment of high-momentum fluid to successfully reattach the flow.

Key words: boundary layer separation, instability, flow control, transition to turbulence

1. Introduction

1.1. *Technical background*

Despite all the advances in our understanding of fluid mechanics during the past century, the two flow phenomena that largely determine the aerodynamic performance of air, sea, and land vehicles – *boundary-layer separation* and *laminar-turbulent transition* – still belong to the least understood areas of flow physics. Although much research has been done over the years on both separation and transition, the flow phenomenon in which both of these mechanisms are present at the same time – the so-called *laminar separation bubble* (LSB) – has received comparatively little attention despite its relevance and importance for various engineering applications.

LSBs typically form when a (laminar) boundary layer detaches from a surface, undergoes transition and eventually reattaches to the surface as a transitional or turbulent flow. Laminar separation is generally associated with a number of undesirable effects such as a loss in lift and a potentially significant increase in drag, especially when the separation bubble is 'long' (versus 'short', see § 1.2). Technical applications which are susceptible to such adverse effects include turbomachinery flows, low-Reynolds-number airfoils and high-lift devices, to name a few.

† Email address for correspondence: faselh@email.arizona.edu

https://doi.org/10.1017/jfm.2011.34 Published online by Cambridge University Press

In recent years, the need for smaller jet engines (such as those used in unmanned aerial vehicles) or jet engines operating at very high altitudes has spawned renewed interest in the problem of laminar separation. This interest is mainly due to the fact that, as the characteristic length scales get smaller (or as the air density decreases during high-altitude cruise), operating Reynolds numbers in low-pressure turbine (LPT) stages can drop to low enough values so that the boundary layers remain laminar, even in the presence of elevated free-stream turbulence. What makes LPT blades particularly prone to laminar separation is the fact that the flow geometry first exposes the suction-side boundary layer to a strong *favourable* pressure gradient, which is followed by a strong *adverse* pressure gradient (APG). The stabilizing effect of the favourable pressure gradient increases the critical Reynolds number (i.e. the Reynolds number above which small-amplitude disturbances are amplified within the boundary layer), thus often preventing transition from occurring 'naturally' upstream of the APG region. Since laminar boundary layers are not able to overcome APGs as well as 'momentum-rich' turbulent boundary layers, the flow separates from the blade. As a consequence, significant losses are incurred in turbine stage efficiency as well as in overall engine performance.

It was recognized several years ago that active flow control (AFC), when applied to LPT blades, could counter such unfavourable conditions, and that AFC could potentially lead to considerable performance improvements as well as to a reduction in component weight. In an experimental research program at the Air Force Research Laboratory (AFRL), Bons, Sondergaard & Rivir (2001, 2002) and Sondergaard, Bons & Rivir (2002) systematically explored the potential of employing AFC for LPT separation. Sondergaard *et al.* (2002) were able to reduce separation-induced wake losses in an LPT cascade at off-design conditions by up to 60 % when so-called vortex generator jets (VGJs) were employed, i.e. when fluid was injected into the boundary layer through a series of small holes (see § 1.3). Bons *et al.* (2001) showed that similar performance improvements could be obtained with only a fraction of the mass flux when pulsed blowing with VGJs was used.

1.2. *Laminar separation bubbles*

Most of the early investigations of LSBs focused on the mean-flow structure, and these investigations were mainly aimed at establishing parameters that govern the formation and size of LSBs (Gaster 1966). Horton (1968) provided a schematic illustration of the mean-flow structure for APG-induced separation, which is reproduced in figure 1. As a result of the APG and the viscous forces, fluid particles in the near-wall region are retarded until their forward motion comes to rest at the separation point, *S*. Just downstream of separation, the fluid within the bubble (i.e. below the separated shear layer) is almost stationary in the so-called dead-air region. Downstream of the 'transition point', denoted in figure 1 as T, the bubble is typically characterized by the presence of the so-called reverse-flow vortex – the region in which the velocity profiles have the strongest reverse-flow percentages. This part of the bubble also exhibits the strongest exchange of momentum with the free stream, which causes the flow to reattach at the point *R*. The 'dividing streamline', i.e. the streamline that connects the points *S* and *R*, thus forms the closed region known as the laminar separation bubble.

As a result of the early investigations of LSBs, separated flows were classified into two main categories: 'short' bubbles and 'long' bubbles. In this classification, which is not necessarily related to the actual length of the bubble (i.e. the distance between the separation and reattachment points), bubbles are considered 'short' if they cause

https://doi.org/10.1017/jfm.2011.34 Published online by Cambridge University Press

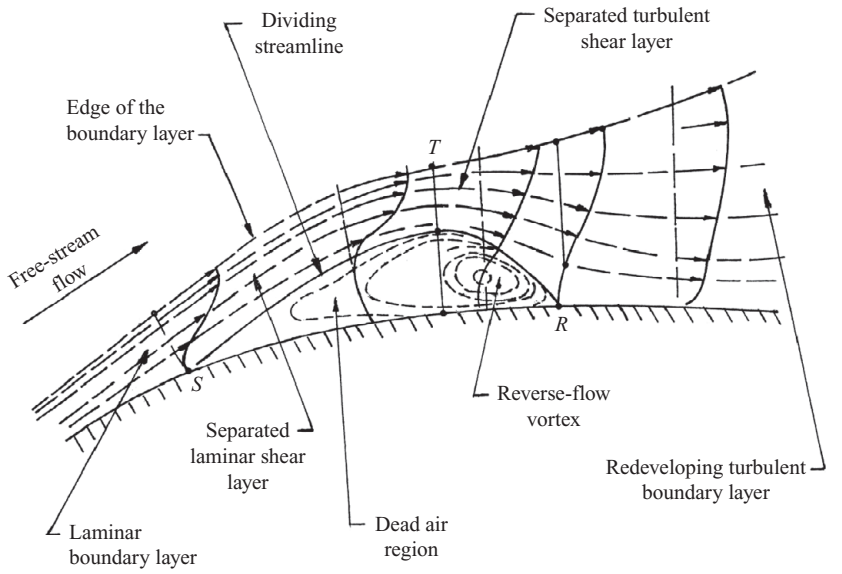


FIGURE 1. Mean-flow structure of a laminar separation bubble. Reproduced from Horton (1968).

only a small deviation from the inviscid pressure distribution. 'Long' bubbles, on the other hand, alter the pressure distribution completely and are therefore detrimental to the aerodynamic performance of airfoils. In fact, in the context of AFC, a particular control strategy can already be considered successful if, as a result of the actuation, a 'long' bubble is transformed into a 'short' one.

Unsteady phenomena associated with laminar separation have only been considered in detail since the late 1980s. Gruber (1987) investigated the onset of unsteady separation and the hydrodynamic stability characteristics of LSBs by means of numerical integration of the two-dimensional, incompressible Navier–Stokes equations. He observed that steady separation could no longer exist beyond a threshold value of separation intensity. Gruber also found that a close connection exists between the hydrodynamic stability characteristics of a separated boundary layer and that of a free shear layer. Pauley, Moin & Reynolds (1990) also studied the unsteady structure of LSBs using numerical solutions of the 2D Navier–Stokes equations. Comparisons with the results of Gaster (1966) were made, and it was suggested that Gaster's 'bubble bursting' (i.e. the sudden transformation from a 'short' separation bubble to a 'long' one) was actually related to the '*demise of unsteady separation*' (Pauley *et al.* 1990).

The 2D computational results of Ripley & Pauley (1993) reproduced the major characteristics of Gaster's experiments (Gaster 1966), such as the separation point, the pressure plateau and the reattachment location. Their numerical results led Ripley & Pauley (1993) to the conjecture that large-scale two-dimensional structures may be responsible for the reattachment of the separated shear layer, and that the transition to turbulence may only play a secondary role in controlling the size of LSBs.

Detailed investigations of the transition process in LSBs, both experimental and computational, have only been conducted in recent years. Among the first of such investigations were those of Pauley (1994) and Rist & Maucher (1994). Pauley (1994) introduced random as well as harmonic 3D disturbances into the 2D separation

https://doi.org/10.1017/jfm.2011.34 Published online by Cambridge University Press

bubble of Pauley *et al.* (1990). In the case of the harmonic 3D disturbance input, the strength of the shed vortices decreased, and the bubble was found to grow in length. Rist & Maucher (1994) investigated the linear and nonlinear stability characteristics of a LSB by studying the development of both 2D and 3D instability waves. Good quantitative agreement was obtained between the numerical results and linear stability theory, which led Rist & Maucher (1994) to conclude that non-parallel effects may only play a minor role in LSB transition.

The numerical studies by Spalart & Strelets (2000) and Alam & Sandham (2000) focused on the turbulent flow following reattachment, but both investigations included some qualitative results regarding possible transition mechanisms in LSBs. Spalart & Strelets (2000) argued that 'the transition mechanism involves the wavering of the shear layer and then Kelvin–Helmholtz vortices, which instantly become three-dimensional without pairing'. Alam & Sandham (2000) considered the flow structures in the transitional and reattaching flow regions and concluded that the transitional region is characterized by the breakdown of large-scale Λ-vortices. Detailed experimental results aimed at providing insight into the physical mechanisms governing the growth of disturbances in a LSB were presented by Watmuff (1999). A small-amplitude impulsive disturbance was introduced into the flow, thus exciting a broad spectrum of frequencies and wavelengths. The initial decay in amplitude of the modes was followed by rapid growth in the separated region. Watmuff (1999) suggested that this growth is due to an inviscid Kevin–Helmholtz instability, eventually leading to the formation of large-scale vortex loops in the vicinity of the reattachment region. Watmuff (1999) also suggested that the two-dimensional vortex shedding of the 'undisturbed' flow was caused by an absolute instability (Huerre & Monkewitz 1990; Schmid & Henningson 2001).

While the amplification of two-dimensional (or weakly oblique) high-frequency disturbances in LSBs due to a Kelvin–Helmholtz instability of the separated shear layer is a well-known and commonly accepted phenomenon, the appearance/growth of longitudinal steady structures has been a more controversial issue. While some researchers suggested a Görtler-type instability (due to local streamwise curvature in the vicinity of boundary-layer separation) as a potential cause for longitudinal vortices (Pauley 1994), others have found no such evidence (Spalart & Strelets 2000). For a LSB on a flat plate subjected to a strong favourable-to-adverse pressure gradient, Marxen *et al.* (2009) detected two fundamental mechanisms: spatial transient growth and a Görtler-type instability. They provide strong evidence that the onset of Görtler-type instability near the start of the APG may indeed be due to streamline curvature.

Direct numerical simulations (DNS) are typically characterized by a low level of background disturbances ('numerical noise'), especially when higher order methods are employed as for our simulations. It has been a long-standing discussion whether the numerical noise originating from round-off and truncation errors in a numerical simulation is sufficient to reproduce 'realistic' separation bubbles as observed in laboratory or free-flight experiments. For high APGs and/or when flow instabilities are of absolute/global nature (see Jones, Sandberg & Sandham 2008 as an example) this can certainly be the case. However, in most cases 'appropriate' forcing upstream of separation is needed in order to match experimental data. While this is typically done by introducing selective or random disturbances *inside* the boundary layer, Balzer & Fasel (2010) use a numerical model for generating isotropic grid turbulence in the free stream.

Even small disturbance input can result in a significant change of the mean flow, i.e. a difference arises between the time-averaged uncontrolled and controlled flows

https://doi.org/10.1017/jfm.2011.34 Published online by Cambridge University Press

(see Marxen & Rist 2010). This is expected to also apply for the situation in the present paper due to the high amplitudes of the disturbance input. The resulting separation bubble is in general shorter and appears to be more stable compared to the uncontrolled, larger separation bubble.

1.3. *Vortex generator jets for active flow control*

According to a classification often used in the literature (Gad-el Hak, Pollard & Bonnet 1998), flow control strategies are either *active* or *passive*, depending on whether an external energy input is required or not required, respectively. While passive flow control is of great technological importance, such strategies are ultimately limited because of their inability to 'adapt' to changing flow conditions. As a result, recent research efforts increasingly focus on developing and/or improving AFC techniques. The present review shall only consider one such strategy, namely that of using the so-called vortex generator jets. VGJs constitute an active control strategy in which fluid is injected into the boundary layer through a spanwise array of small holes. The VGJ injection direction (see figure 5) is typically characterized by a skew angle (formed by the projection of the jet onto the surface and the free-stream direction) and a pitch angle (formed by the jet and its projection onto the surface).

Most of the research conducted on VGJs has involved jets issuing into turbulent boundary layers. Pulsed VGJs were first considered by McManus, Legner & Davis (1994), McManus *et al.* (1995). The jets were reported to successfully prevent separation in an otherwise stalled two-dimensional diffuser (McManus *et al.* 1994), and it was suggested that pulsing leads to the formation of large-scale streamwise structures which promote mixing in the turbulent boundary layer. In comparison to steady VGJs, the pulsed jets improved separation control significantly for a fixed mass flux. Furthermore, in experiments performed on a flat-plate model geometry (McManus *et al.* 1995), pulsed VGJs delayed stall for larger angles of attack than steady VGJs. In an effort to shed light on the physical mechanisms relevant in pulsed jet separation control, Johari & McManus (1997) investigated the interaction of pulsed VGJs with a zero-pressure-gradient turbulent boundary layer from the perspective of vorticity dynamics. They attributed the improved performance of pulsed VGJs (compared to steady VGJs) to the formation, stretching and bending of vortex ring-like structures. The conjecture that large-scale vortex rings may be responsible for the improved performance of pulsed VGJ control for *turbulent* flows was corroborated by the experiments of Johari & Rixon (2003), who investigated the effects of pulsing on a single VGJ injected into a zero-pressure-gradient, turbulent boundary layer. The pulsed jet generated a start-up vortex ring, followed by a pair of counter-rotating streamwise vortices. In comparison to steady jets with the same velocity, pulsed jets were found to penetrate 'deeper' into the boundary layer. In other words, the placement of the flow structures farther out in the boundary layer was proposed as the essential physical mechanism that improved the effectiveness of pulsed jets compared to steady jets.

Control of *laminar* separation using VGJs has only been considered by a relatively small number of researchers, a few were already mentioned in § 1.1. The experimental investigations of Bons *et al.* (2001, 2002) and Sondergaard *et al.* (2002) at AFRL focused on controlling laminar separation for LPT blades. In these experiments, AFC using VGJs resulted in a drastic reduction in boundary-layer separation at low chord Reynolds numbers ($25\,000 \leqslant Re \leqslant 100\,000$). The jets were employed at a skew angle of 90° and a pitch angle of 30°. Various jet amplitudes and duty cycles (ratio of jet on-time to pulsing period) were investigated, and both steady and pulsed blowing

https://doi.org/10.1017/jfm.2011.34 Published online by Cambridge University Press

were reported to be effective in reducing separation losses. However, pulsed blowing was shown to be much more efficient, requiring only a small fraction of the mass flux compared to the steady VGJs. Bons *et al.* (2002) attributed the significant impact of VGJ control to a combined effect of free-stream momentum entrainment (due to longitudinal vortices) and an accelerated boundary-layer transition, especially when the jets were employed near the separation location of the uncontrolled flow. For more realistic turbine flow environments with upstream generated periodic wakes, Bloxham *et al.* (2007) showed that pulsed VGJs can be synchronized with the passing wakes to obtain an optimal separation control.

In order to decrease weight and hardware cost of modern LPTs, the use of high-lift airfoils has received much attention over the past decade. However, 2D and even more so 3D losses were found to contribute to an overall decrease in efficiency when using high-lift airfoils (see Gier *et al.* 2008, for example). It was shown by Bons *et al.* (2005) that such losses can be recovered and more aggressive LPT blades are possible when VGJ control is considered already in the design process.

Although the experiments at AFRL have convincingly demonstrated that VGJs (both steady and unsteady) can be employed successfully for preventing LPT separation and stall, the relevant physical mechanisms are far from understood. In other words, the questions: 'Why are VGJs so effective in reducing/eliminating boundary-layer separation?' and in particular 'Why are *pulsed* VGJs so much *more* effective?' have yet to be answered, and these are precisely the questions that have motivated the present investigation.

Since LSBs are essentially low-Reynolds-number phenomena, they lend themselves to investigations using DNS. In this paper, the following 'model problem' is considered: a laminar boundary layer on a flat plate is subjected to the same streamwise pressure gradient as measured on an actual LPT blade, thereby reducing the complexity of the geometry such as surface curvature, blade trailing edge, etc. As a result, all the available computational resources can be concentrated in the area of primary interest (i.e. the separated flow region), thus allowing for highly resolved simulations. In fact, in the present simulations, all relevant length scales are sufficiently resolved, and the numerical results are 'converged' in that a further refinement of the computational grid does not cause any significant changes in the solution (see Appendix A). Consequently, the present investigations provide an unprecedented level of detail regarding the flow structures that develop as a result of VGJ control, in general, and pulsed VGJ control, in particular.

2. Numerical method

2.1. *Governing equations*

The incompressible, unsteady Navier–Stokes equations form the set of governing equations for the present investigation:

$$\nabla \cdot \boldsymbol{v} = 0 \tag{2.1a}$$

$$\frac{\partial \boldsymbol{v}}{\partial t} + (\boldsymbol{v} \cdot \nabla)\,\boldsymbol{v} = -\nabla p + \frac{1}{Re}\nabla^2 \boldsymbol{v}. \tag{2.1b}$$

Equations (2.1*a*) and (2.1*b*) are non-dimensionalized with a global reference velocity, U_∞, and a reference length, L:

$$\nabla = L\nabla^*; \quad t = \frac{t^* U_\infty}{L}; \quad \boldsymbol{v} = \frac{\boldsymbol{v}^*}{U_\infty}; \quad p = \frac{p^* - p^*_\infty}{\rho U_\infty^2}. \tag{2.2}$$

https://doi.org/10.1017/jfm.2011.34 Published online by Cambridge University Press

In this paper, the Navier–Stokes equations are considered in the vorticity–velocity formulation, which is obtained by taking the curl of the momentum equation (2.1*b*) and by taking into consideration the fact that both velocity and vorticity vectors are solenoidal:

$$\frac{\partial \boldsymbol{\omega}}{\partial t} + (\boldsymbol{v}\cdot\nabla)\,\boldsymbol{\omega} = (\boldsymbol{\omega}\cdot\nabla)\,\boldsymbol{v} + \frac{1}{Re}\nabla^2\boldsymbol{\omega} \tag{2.3a}$$

$$\nabla^2\boldsymbol{v} = \nabla\times\boldsymbol{\omega}. \tag{2.3b}$$

In contrast to the primitive-variable formulation, (2.1*a*) and (2.1*b*), the vorticity–velocity formulation of the governing equations has the distinct advantage in that the pressure term does not appear as a dependent variable. As a result, the vorticity–velocity formulation alleviates some of the difficulties associated with the lack of an evolution equation for the pressure in the primitive-variable formulation. Ever since the work of Fasel (1976), several researchers have successfully employed the vorticity–velocity formulation for the numerical solution of the incompressible Navier–Stokes equations (for a review, see Meitz & Fasel 2000 or Davies & Carpenter 2001).

In the following, the present DNS method shall only be outlined very briefly. For a more detailed discussion as well as validation results, the reader is referred to Meitz & Fasel (2000) and Postl & Fasel (2006).

2.2. *Spatial discretization*

The spatial derivatives in the streamwise (x) and the wall-normal (y) direction are discretized using fourth-order accurate split compact differences, which provide improved wave-resolution characteristics at no additional cost compared to standard compact differences (Lele 1992). The spanwise (z) direction is assumed to be periodic, as a result of which the flow field is expanded in Fourier cosine and sine series. Each variable is represented by a total of $2K+1$ Fourier modes: the 2D spanwise average (zeroth Fourier mode), K symmetric Fourier cosine as well as K antisymmetric Fourier sine modes:

$$\omega(x,y,z,t) = \Omega_0(x,y,t) + \sum_{k=1}^{K}\Omega_k(x,y,t)\cos(\gamma_k z) + \sum_{k=K+1}^{2K}\Omega_k(x,y,t)\sin(\gamma_k z). \tag{2.4}$$

2.3. *Time integration*

The time integration of the governing equations is performed using an explicit, four-stage, fourth-order accurate Runge–Kutta scheme (Ferziger 1998). At each stage of the Runge–Kutta integration, the following computational steps are performed.

(i) Compute the nonlinear terms in the vorticity-transport equation. These terms are evaluated pseudo-spectrally, i.e. they are calculated using at least $3K$ spanwise collocation points in physical space to avoid aliasing errors (Orszag 1971).

(ii) Integrate (2.3*a*) over one Runge–Kutta step.

(iii) Solve (2.3*b*) for the wall-normal velocity at the new time level.

(iv) Compute the spanwise and streamwise velocity components at the new time level. For each of these variables, (2.3*b*) reduces to an ordinary differential equation for each grid line $j = \text{const}$.

(v) Compute the wall-vorticity components $\Omega_{x,k}$ and $\Omega_{y,k}$ from the velocity field.

https://doi.org/10.1017/jfm.2011.34 Published online by Cambridge University Press

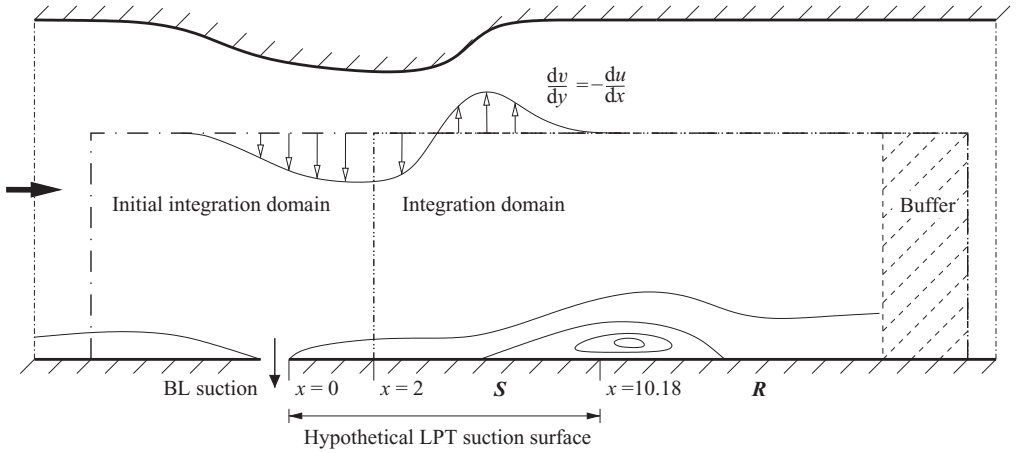


FIGURE 2. Schematic illustration of the computational set-up. BL suction, boundary-layer suction.

2.4. *Boundary conditions*

At the inflow boundary, all velocity and vorticity components are prescribed as Dirichlet conditions. For maintaining the fourth-order accuracy of the code, the streamwise derivatives are prescribed as well. To prevent reflections from the outflow boundary, turbulent fluctuations are damped out in a buffer domain using the approach proposed by Meitz & Fasel (2000). At the upper boundary, a Neumann condition is prescribed for the wall-normal velocity, $\partial v/\partial y = f(x)$, and irrotational flow is assumed, $\boldsymbol{\omega} = 0$. Since the equations for the streamwise (u) and spanwise (w) velocity components reduce to ordinary differential equations in the streamwise direction, no free-stream boundary conditions are required for these variables. At the wall, no-slip and no-penetration conditions are imposed, except at locations where disturbances are introduced (see § 3.2).

3. Simulation set-up

The first step in setting up the present simulations involves 'unrolling' the suction surface of a LPT blade onto a flat plate. The computational set-up is illustrated schematically in figure 2. Shown are the integration domain used for a precursor calculation and the domain used for the actual simulations. In the precursor calculation, a Blasius boundary layer with $Re_{\delta_1} \approx 100$ is specified at the inflow. The flow is accelerated in a region with a strong favourable pressure gradient, and suction at the wall is employed to generate a 'new' boundary layer at the leading edge of the hypothetical LPT suction surface ($x = 0$). The resulting boundary-layer profile at $x = 2$ is used as an inflow condition for subsequent simulations in which an APG is imposed downstream of the accelerated region. The streamwise pressure gradient that is imposed at the free-stream boundary is adjusted iteratively until both the wall-pressure distribution and the intensity (i.e. the height) of the separation region are in good qualitative agreement with the experimental measurements for a LPT blade by Bons *et al.* (2001, 2002) and Sondergaard *et al.* (2002).

3.1. *Uncontrolled flow*

A comparison between the calculation results and the experimental measurements for the uncontrolled flow is presented in figure 3. Shown are distributions of the

https://doi.org/10.1017/jfm.2011.34 Published online by Cambridge University Press

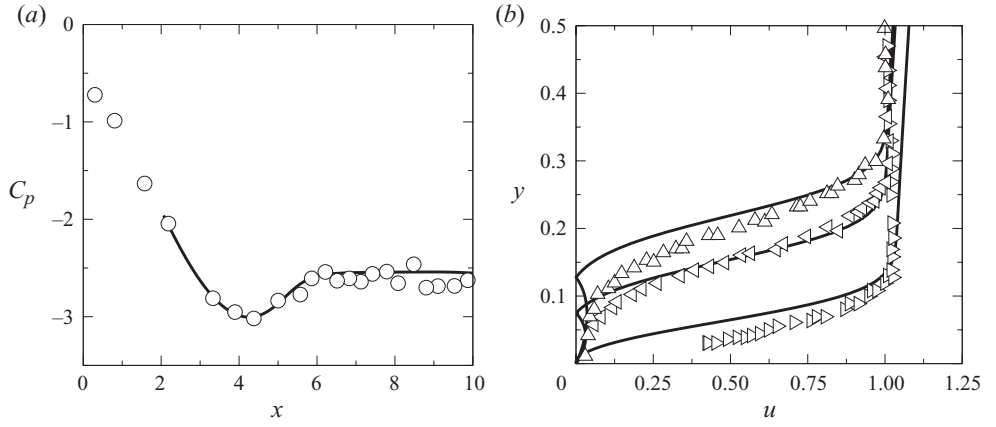


FIGURE 3. Comparison of simulation results with experimental data for the uncontrolled flow. (*a*) Wall-pressure coefficient, C_p, and (*b*) streamwise velocity profiles, u. Lines: simulation results; symbols: experimental measurements. (▷) $x \approx 5.6$; (◁) $x \approx 6.4$; (△) $x \approx 6.7$.

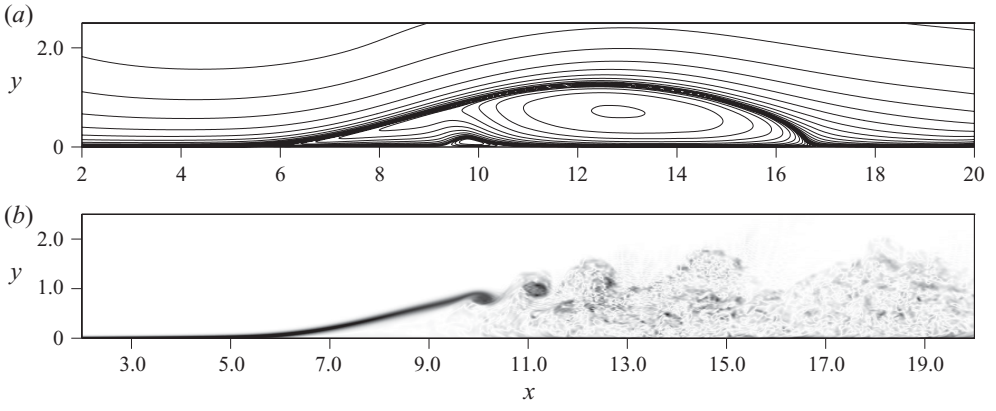


FIGURE 4. Typical simulation results for the uncontrolled flow. (*a*) Streamlines (equidistant contours of $\ln(|10^4 \times \psi| + 1)$) and (*b*) instantaneous grey-scale contours of the spanwise vorticity component (averaged in the spanwise direction).

wall-pressure coefficient, C_p, and the streamwise velocity profiles, u. The pressure plateau downstream of $x \approx 6$ represents the 'dead-air' region in the separation bubble (cf. figure 1). The qualitative agreement between the velocity profiles at the various streamwise locations indicates that the separation bubble created by the acceleration/deceleration at the free stream is indeed representative of the flow characteristics encountered in LPT applications. It should be noted, however, that many factors which play an important role in turbomachinery flow such as the effect of curvature, the blade trailing edge (and thus circulation), high level of free-stream turbulence and passing wakes are neglected in our current model.

Typical results obtained from the simulations of the uncontrolled flow using $801 \times 129 \times 80$ gridpoints (see Appendix B, case *UNF*) are presented in figure 4. Shown are streamlines of the time-averaged flow field (*a*) and instantaneous contours of the spanwise vorticity component (*b*). The grid resolution was such that all relevant scales in the transition process and turbulent flow are sufficiently resolved. The

https://doi.org/10.1017/jfm.2011.34 Published online by Cambridge University Press

laminar boundary layer separates from the wall, undergoes transition and eventually reattaches to the surface. The mean separation and reattachment locations are $x \approx 5.6$ and $x \approx 16.9$, respectively. Since the trailing edge of the hypothetical LPT suction surface is located at $x \approx 10$, the unforced flow through a real LPT cascade would, for this case, not reattach to the blade. The instantaneous vorticity contours illustrate the initial 'roll-up' of the separated shear layer and the shedding of strongly two-dimensional vortical structures. A stability analysis (see Postl 2005, for details) of the time- and spanwise-averaged velocity profiles with the largest reverse-flow percentage (approximately 26 % at $x \approx 13.2$) showed that the (uncontrolled) separation bubble is convectively unstable. This observation is particularly interesting in that for the same Reynolds number Alam & Sandham (2000) predict the presence of an absolute instability for reverse flows in excess of 15 %. However, even without the presence of an absolute mechanism, the large amplification rates associated with the strong hydrodynamic instability of the velocity profiles with respect to two-dimensional disturbances lead to self-sustained vortex shedding (although our method is fourth-order accurate and the simulations are highly resolved). The non-dimensional 'natural' frequency associated with this vortex shedding is $f \approx 0.77$, which was obtained by analysing time traces of the flow variables in the vicinity of the shear-layer roll-up. This frequency, when expressed in terms of the Strouhal number based on the local free-stream velocity and the momentum thickness at separation, takes on a value of $St_\theta \approx 7.3 \times 10^{-3}$. As such, St_θ in the present case is only approximately 6 % larger than the 'universal' value found by Pauley *et al.* (1990).

The shedding frequency of the uncontrolled separation bubble is relevant for the controlled simulations discussed in §§ 4 and 5.

3.2. *Disturbance generation: vortex generator jets*

The VGJs are modelled by specifying appropriate boundary conditions of the velocity and vorticity components at the wall. Note that only one VGJ hole centred at $(x, z) = (5.0, 0.0)$ is computed within spanwise periodic boundaries of the computational domain. Depending on the angle at which fluid is injected into the flow, the VGJ 'hole shape' changes from circular to elliptical which follows from the effect of actually 'drilling' a hole into the surface at an angle. The VGJ injection direction is typically characterized by the pitch angle, φ, and the skew angle, θ (see figure 5*a*). The pitch angle is formed by the jet vector and its projection onto the surface; the skew angle is formed by the projection of the jet vector onto the surface and the x-axis.

For the purpose of illustrating the implementation of the VGJs, consider a hole drilled vertically into the wall (i.e. with a pitch angle of 90°). The velocity distribution at the wall is then modelled by a $\cos^3$-distribution, $v_{jet} = \cos(\pi/2 \times r/D)^3$, where D is the actual hole diameter. Although this distribution does not fully resemble the desired Poiseuille-type profile (see figure 5*b*), the present high-order numerical method (i.e. the compact differences and the pseudo-spectral treatment of the spanwise direction) requires that the prescribed velocity distribution have continuous derivatives at $r/D = 1$. As a result, an 'equivalent' hole diameter ($\mathscr{D} \approx 0.66\ D$) is introduced based on a Poiseuille distribution with the same mass flux. The equivalent hole diameter is $\mathscr{D} = 0.1$ (or $\mathscr{D}^* = 2.54$ mm) which is larger than that in the experiments by Bons *et al.* (2002) ($D^* = 1$ mm). The hole spacing of $9\mathscr{D}$ is slightly smaller than that in the experiments ($10D$). A larger hole diameter and a slightly smaller hole spacing were chosen due to limitations of available computational resources. The 'equivalent' hole

https://doi.org/10.1017/jfm.2011.34 Published online by Cambridge University Press

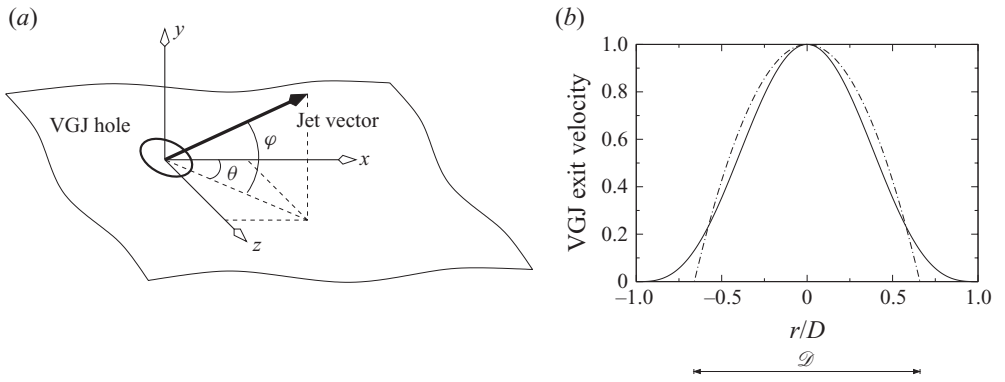


FIGURE 5. (*a*) Schematic illustration of the VGJ injection and (*b*) VGJ exit velocity profile for vertical jet injection: (—) actual distribution; (— · —) Poiseuille distribution.

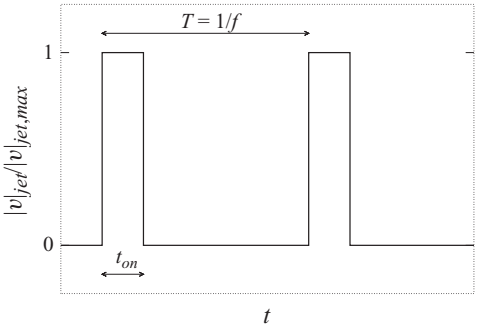


FIGURE 6. Schematic illustration of pulsed VGJ actuation.

diameter $\mathscr{D}$ is subsequently used for evaluating characteristic quantities such as the ratio of boundary-layer thickness to VGJ hole diameter.

The strength of the VGJ forcing is characterized by the following two quantities: (i) the jet blowing ratio and (ii) the jet momentum coefficient. The jet blowing ratio, B, is defined as the ratio of the maximum jet exit velocity to the global reference velocity:

$$B = \frac{v_{jet,max}}{U_\infty}. \tag{3.1}$$

The jet momentum coefficient, C_μ, is defined as

$$C_\mu = \tau \frac{\pi \mathscr{D}^2 v_{jet,max}^2}{4 A_{ref} U_\infty^2}, \tag{3.2}$$

where A_{ref} is a characteristic reference area. The duty cycle, τ, in (3.2) is defined as the ratio of the jet 'on-time' to the forcing period (see figure 6):

$$\tau = t_{on}/T. \tag{3.3}$$

https://doi.org/10.1017/jfm.2011.34 Published online by Cambridge University Press

Case	φ	θ	B	f	τ	$\mathscr{D}$	$\mathscr{D}/\delta$
SV-A	90°	0°	0.316	N/A	N/A	0.1	0.78
SA-A	30°	−90°	0.316	N/A	N/A	0.1	0.78
PV-A	90°	0°	1	0.77	10 %	0.1	0.78
PA-A	30°	−90°	1	0.77	10 %	0.1	0.78
TRIP	N/A	N/A	N/A	N/A	N/A	N/A	N/A
UNF	N/A	N/A	N/A	N/A	N/A	N/A	N/A

TABLE 1. Overview of the cases presented in § 4.

4. Comparison of selected cases with VGJ control

Cases presented and discussed in this section were chosen to expose the significant differences in the effectiveness of VGJ control, depending on the configuration in which the jets are employed (e.g. steady versus pulsed or vertical versus angled injection). Time-averaged results of selected controlled cases emphasize the motivation for more detailed investigations of the relevant physical mechanisms associated with pulsed VGJs. Four cases involving VGJ control are considered:

(i) steady, vertical injection (case *SV*-A);
(ii) steady, angled injection (case *SA*-A);
(iii) pulsed, vertical injection (case *PV*-A);
(iv) pulsed, angled injection (case *PA*-A).

The jet injection location is at $x_{jet} = 5$. As in the experiments, the pitch angle is $\varphi = 30°$ and the skew angle is $\theta = -90°$ (i.e. VGJ injection in the negative z-direction) for the cases where the VGJs are employed at an angle. The ratio of the hole diameter to the local boundary-layer thickness is $\mathscr{D}/\delta \approx 0.78$. The forcing frequency for the pulsed cases is the same as the 'natural' shedding frequency of the unforced shear layer, $f = 0.77$. The duty cycle of the pulsing is $\tau = 10\,\%$. The blowing ratio, B, is such that the jet momentum coefficient has a constant value of $C_\mu = 1.2 \times 10^{-4}$ for all cases. Since the jet momentum coefficient is related to the 'energy input' that is required for controlling the flow, the four cases presented here shed light not only on the effectiveness but rather also on the efficiency of the various VGJ strategies. In addition to the cases with VGJ control, results are also presented for a case in which the boundary layer is tripped to 'turbulence' upstream of the separation location (case *TRIP*). This tripping of the boundary layer, using high-amplitude 3D disturbances, suppresses separation altogether and results in attached flow along the entire surface. The cases presented in this section are summarized in table 1. For details on the numerical resolution, including results from a grid study, see Appendix A.

Streamlines of the time- and spanwise-averaged flow fields are presented in figure 7. In addition to the cases with VGJ control, the unforced, 'natural', case (case *UNF*) is included for comparison. For each of the forced cases, there is a significant reduction in the size of the separation bubble. However, the extent to which the separated flow region is reduced in comparison to the unforced case is highly dependent on the VGJ strategy. For the forcing parameters that were chosen in the present cases, steady injection (cases *SV*-A and *SA*-A) is significantly less effective than pulsed injection (cases *PV*-A and *PA*-A). The VGJ injection angle can also be seen to have a considerable effect. While angled VGJ injection is more effective than vertical for steady blowing, the opposite appears to be the case for pulsed blowing. Note that keeping C_μ constant leads to an approximately three times larger (instantaneous) blowing ratio for pulsed actuation compared to steady actuation. Increasing the

https://doi.org/10.1017/jfm.2011.34 Published online by Cambridge University Press

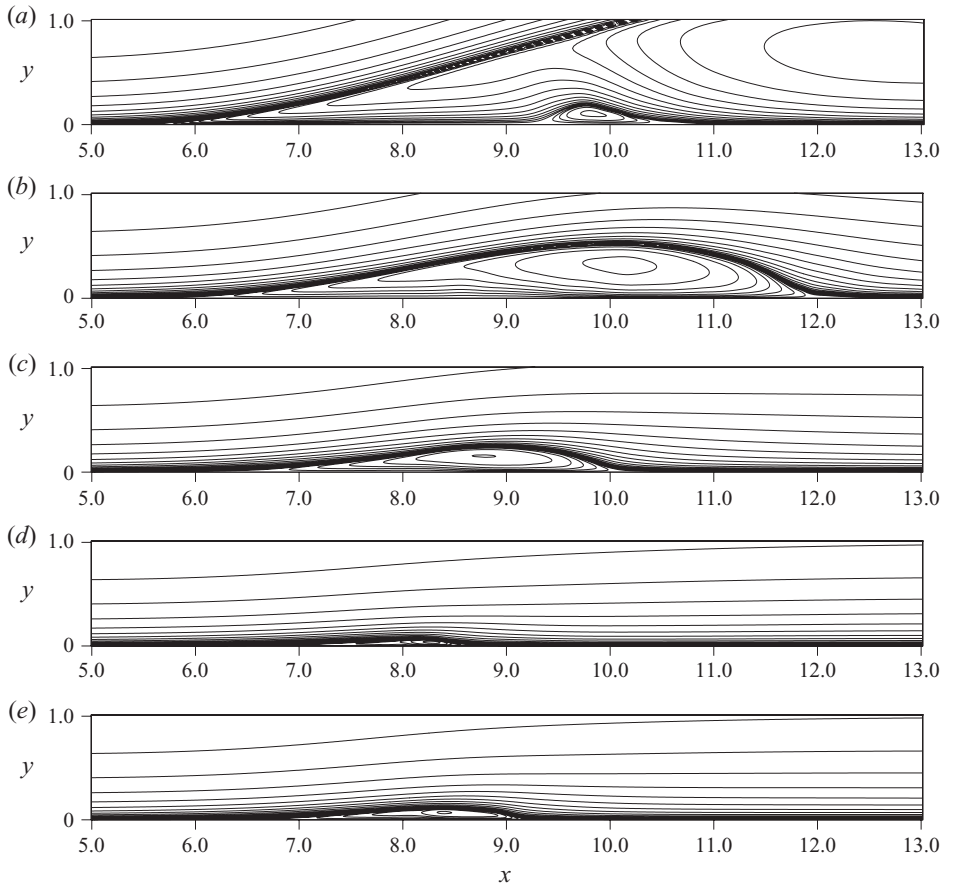


FIGURE 7. Time- and spanwise-averaged streamlines. Plotted are equidistant contours of $\ln(|10^4 \times \psi| + 1)$. (*a–e*) Case *UNF*, case *SV*-A, case *SA*-A, case *PV*-A and case *PA*-A.

blowing ratio to $B = 1$ for steady actuation was found to increase the effectiveness (see Postl 2005). Comparing steady VGJs to pulsed VGJs with the same blowing ratio ($B = 1$), the effectiveness of steady and pulsed actuation was similar for angled VGJ injection but still lower for steady vertical VGJ injection than for pulsed vertical injection.

The control effectiveness of the various VGJ configurations can also be quantified by considering distributions of the mean displacement thickness as well as of the wall-pressure coefficient. These quantities are presented in figure 8. The slightly shallower separation bubble in case *PV*-A (compared to case *PA*-A) can now be identified more clearly than in figure 7. The wall-pressure distributions in figure 8(*b*) provide another direct measure for the effectiveness of the various control strategies. As expected, the C_p-curves approach the 'inviscid' pressure distribution associated with case *TRIP* as the separation bubbles get smaller. The 'kink' in the C_p-curve of case *TRIP* at $x \approx 3$ is a result of the very strong forcing that is required to transition the boundary layer in order to prevent separation. The low Reynolds number as well as the strong favourable pressure gradient renders the flow hydrodynamically *stable* upstream of the APG region. Thus, it should be obvious that case *TRIP* should be considered only as a valuable *reference* case, as tripping of a highly accelerated, low-Reynolds-number boundary layer is not an efficient strategy of controlling the flow.

https://doi.org/10.1017/jfm.2011.34 Published online by Cambridge University Press

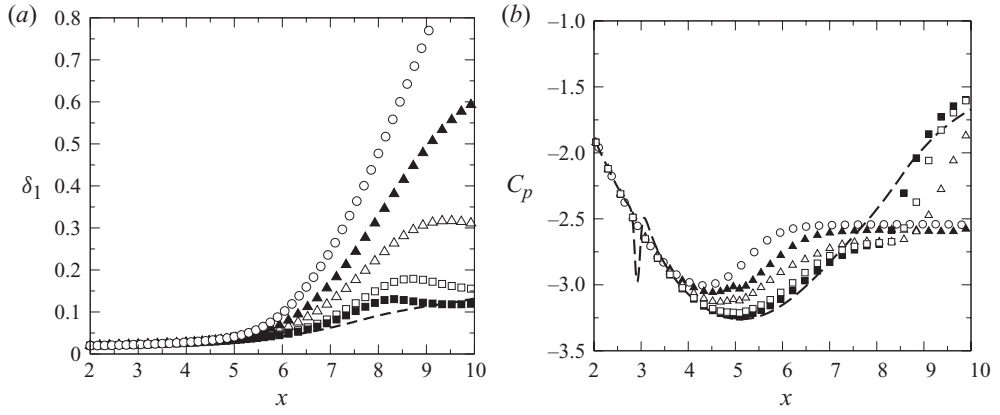


FIGURE 8. Comparison of simulation results for various VGJ control parameters. (*a*) Time- and spanwise-averaged displacement thickness and (*b*) time- and spanwise-averaged wall-pressure coefficient. (○) Case *UNF*; (▲) case *SV*-A; (△) case *SA*-A; (■) case *PV*-A; (□) case *PA*-A and (——) case *TRIP*.

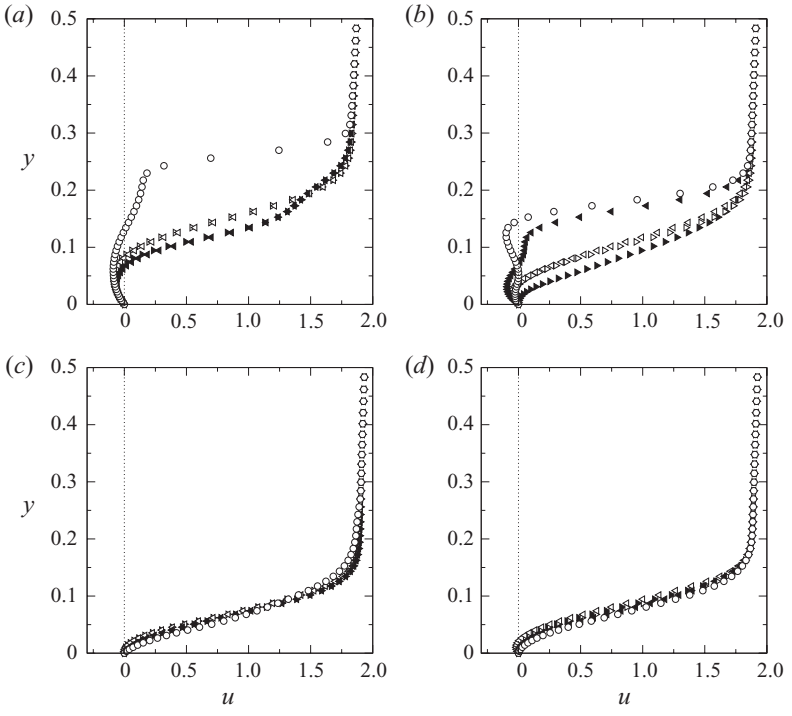


FIGURE 9. Time-averaged streamwise velocity (u) profiles at $(x - x_{jet})/\mathscr{D} = 20$ ($x = 7$) and selected spanwise locations. (*a–d*) Case *SV*-A, case *SA*-A, case *PV*-A and case *PA*-A. (◁) $z/\mathscr{D} = -2$; (◀) $z/\mathscr{D} = -1$; (○) $z/\mathscr{D} = 0$; (▶) $z/\mathscr{D} = 1$; (▷) $z/\mathscr{D} = 2$.

A comparison of streamwise velocity profiles at $(x - x_{jet})/\mathscr{D} = 20$ ($x = 7$) is presented in figure 9. In each of the four graphs, velocity profiles are plotted at various spanwise locations: $z/\mathscr{D} = -2$, $z/\mathscr{D} = -1$, $z/\mathscr{D} = 0$, $z/\mathscr{D} = 1$ and $z/\mathscr{D} = 2$. Of particular interest in figure 9 is the observation that the profiles for steady VGJ actuation exhibit the

https://doi.org/10.1017/jfm.2011.34 Published online by Cambridge University Press

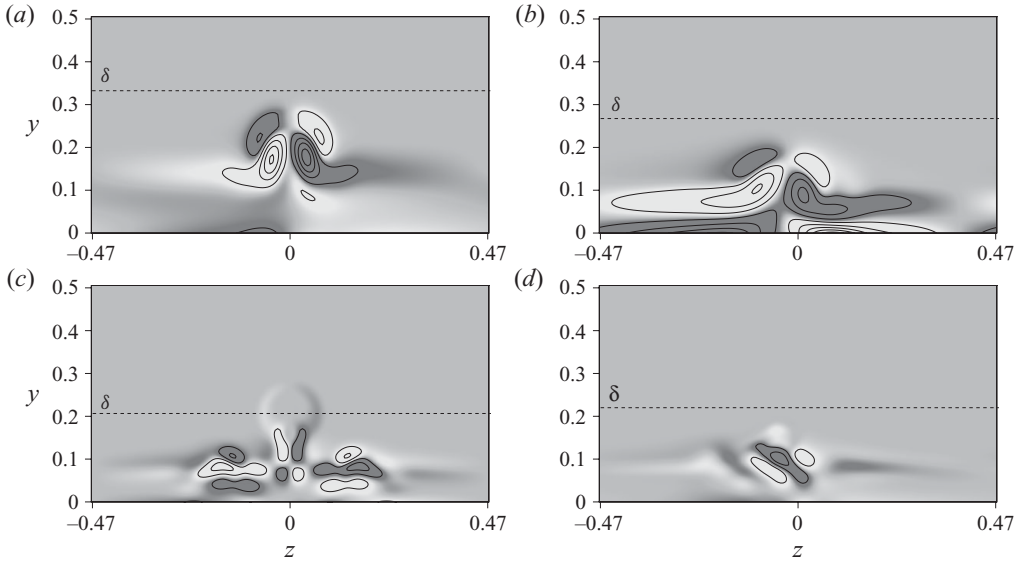


FIGURE 10. Time-averaged streamwise vorticity (ω_x) contours at $(x - x_{jet})/\mathscr{D} = 20$ $(x = 7)$ (looking in the downstream direction). The dark areas represent clockwise rotation, and the bright areas represent counter-clockwise rotation. (*a–d*) Case *SV*-A, case *SA*-A, case *PV*-A and case *PA*-A. (——) spanwise-averaged boundary-layer thickness, δ.

inflectional character that is indicative of longitudinal vortices. In contrast, for the pulsed cases, no significant variation is present in the velocity profiles. This difference provides clear evidence that the physical mechanism responsible for the control of the flow must be different for pulsed VGJs than for steady VGJs. The streamwise vorticity contours shown in figure 10 further corroborate this conjecture.Plotted are grey-scale contours of ω_x in the y/z-plane at $(x - x_{jet})/\mathscr{D} = 20$ $(x = 7)$ for cases *SV*-A, *SA*-A, *PV*-A and *PA*-A (the observer is looking in the downstream direction). The longitudinal vortices alluded to previously are now clearly visible for the two cases with steady VGJ actuation. Results obtained from a local Görtler stability analysis indicated that streamline curvature of the LSB may be the cause for the growth of these longitudinal vortices (see Postl 2005 and discussion in §1.2). For the pulsed cases, on the other hand, the streamwise structures are not only much weaker, but they actually decay in the downstream direction (not shown).

The topology of the flow structures associated with pulsed VGJs, and the different physical mechanisms when compared to steady VGJs, is discussed in more detail in the next section.

5. Pulsed vortex generator jets

5.1. *Vertical versus angled injection*

The time-averaged effects of using pulsed VGJ forcing for cases *PV*-A and *PA*-A were already discussed in §4. Focus is now directed on the unsteady phenomena, in an effort to elucidate the possible role of the dominant unsteady structures for the increased effectiveness of pulsed blowing (compared to steady blowing).

https://doi.org/10.1017/jfm.2011.34 Published online by Cambridge University Press

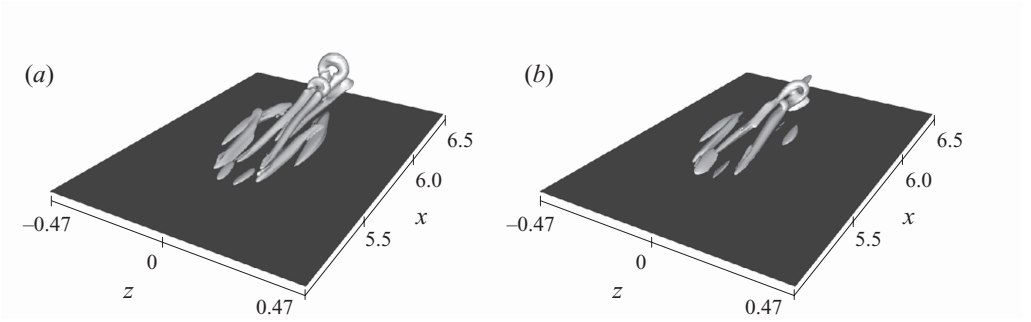


FIGURE 11. Instantaneous flow structures immediately downstream of jet injection ($x = 5$, $z = 0$). Iso-surfaces of $\lambda_2 = -5$ for $B = 1$ at $t/T = 0.7$. (*a*) Case *PV*-A and (*b*) case *PA*-A (jet exit vector pointing in the $-z$ direction).

5.1.1. *Flow structures*

The flow structures that are generated immediately downstream of the jet injection location are considered first. Iso-surfaces of $\lambda_2 = -5$ (using the λ criterion by Jeong & Hussain 1995, for identification of vortical structures) are presented in figure 11 for both cases *PV*-A (*a*) and *PA*-A (*b*). For clarity, only a small part of the computational domain is shown. For the case with vertical VGJs, initially the flow structures closely resemble the prototypical hairpin vortices observed in the investigation of Haidari & Smith (1994), who studied the generation and regeneration of single hairpin vortices created by injection of fluid through a narrow slot. Based on the results of an extensive parametric study, in which the characteristics of both the injection and the approaching boundary layer were varied, Haidari & Smith (1994) identified three regimes for the generation of hairpin vortices: (i) critical, (ii) subcritical and (iii) supercritical. The critical regime was defined as the range of flow/injection conditions which lead to the formation of a *single* hairpin structure. In the subcritical regime, hairpin vortices could not be sustained, while in the supercritical regimes, multiple structures were observed.

In the present investigation, an attempt was made to try and categorize the flow conditions in a similar way as suggested by Haidari & Smith (1994) by using the hole diameter instead of the slot width. The resulting 'equivalent' injection Reynolds number for case *PV*-A, for example, is one order of magnitude higher than any of the injection Reynolds numbers for which Haidari & Smith (1994) were able to obtain *single* hairpin vortices. Therefore, it would appear that the vortices in the present cases should grow and regenerate, as observed in the late stages of Klebanoff-type transition scenarios (Rist & Fasel 1995; Bake, Meyer & Rist 2002). The flow structures in case *PV*-A do indeed exhibit some of the same characteristic features observed by Bake *et al.* (2002), such as the 'bridges' that connect the legs of the structures before evolving into the 'head' of a new hairpin vortex. However, the generation process of additional hairpin vortices and secondary flow structures does not 'continue' in case *PV*-A as it would in the late stages of transition in a zero-pressure-gradient boundary layer. In fact, the strength of the vortices decays as they propagate downstream, suggesting that the structures generated by the pulsed injection may not be the *primary* cause for the effective control of the separation. In other words, for the present flow conditions and forcing parameters, a 'by-pass' transition of the boundary layer (Morkovin 1969) may be ruled out as the most relevant physical mechanism.

https://doi.org/10.1017/jfm.2011.34 Published online by Cambridge University Press

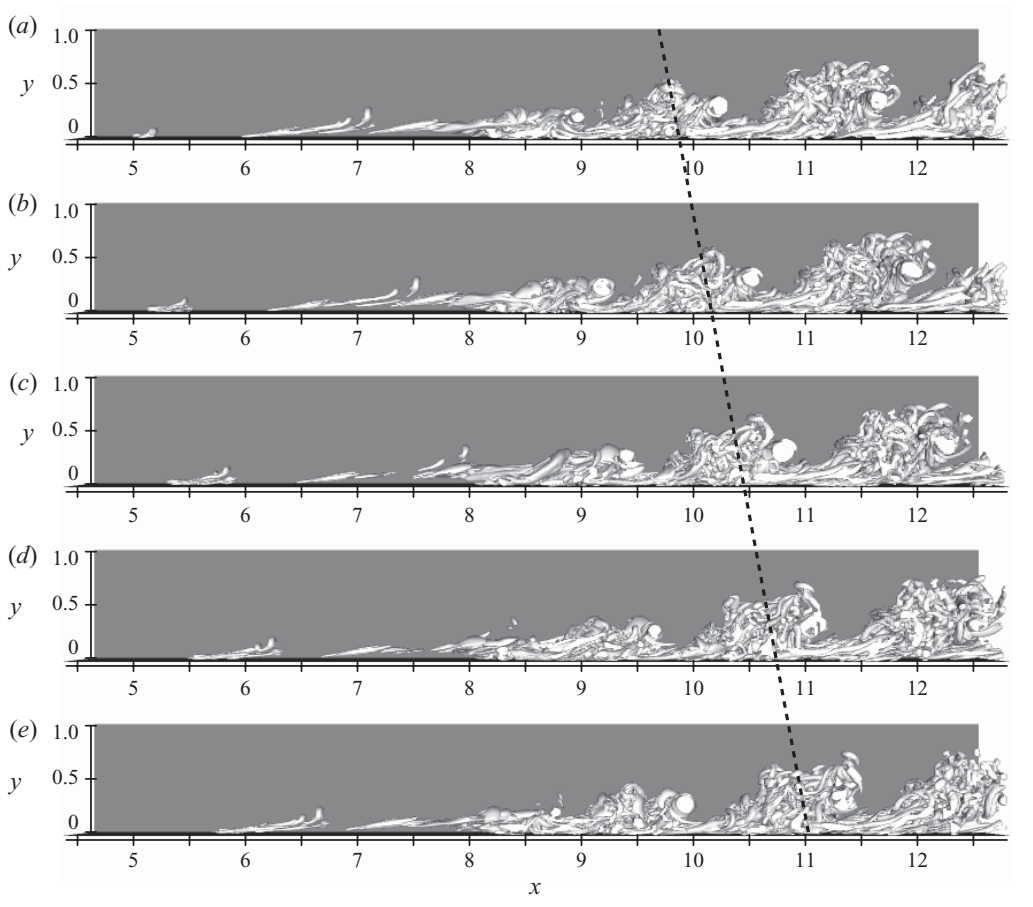


FIGURE 12. Iso-surfaces of $\lambda_2 = -5$ for $B = 1$ at five instances during one forcing period (side view). (*a–e*) $t/T = 0.1$, $t/T = 0.3$, $t/T = 0.5$, $t/T = 0.7$ and $t/T = 0.9$. Case *PV*-A. An animation of this case is provided in supplementary movie 1 available with the online version of the paper at journals.cambridge.org/flm.

Of particular interest for the present study is a more detailed understanding of the flow characteristics in the transitional and early turbulent stages prior to as well as after reattachment. Towards that end, the present pulsed cases are scrutinized with regard to the possible existence and potential role of large coherent structures, i.e. ordered large-scale motion in turbulent flow (Liu 1989). The instantaneous λ_2 side views of figure 12 (case *PV*-A) convincingly illustrate the presence of such ordered motions, and the downstream propagation of one of these structures is highlighted by the dashed line.

Wall traces of the spanwise coherent vortices for both pulsed cases can be seen by plotting space–time diagrams of the skin-friction coefficient (see figure 13). For $x > 6.0$, a variation of the skin-friction coefficient with a distinct time scale becomes visible. The contour lines have a positive slope in the x–t-diagram indicating that the disturbances are travelling in the downstream direction. Moreover, these periodic contour variations are synchronized with the pulsed jet actuation.

While the existence of coherent structures in turbulent flows is nothing new, the observation that their generation and development may be connected to the pulsed

https://doi.org/10.1017/jfm.2011.34 Published online by Cambridge University Press

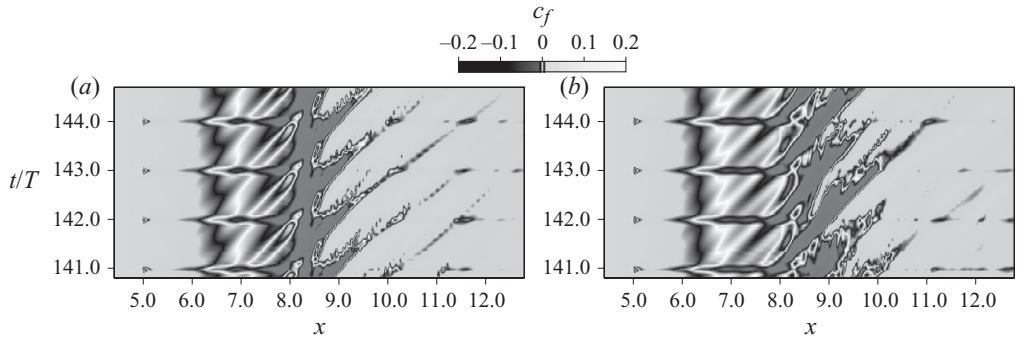


FIGURE 13. Space–time diagrams of spanwise-averaged skin-friction coefficient, c_f. (*a*) Case *PV*-A and (*b*) case *PA*-A.

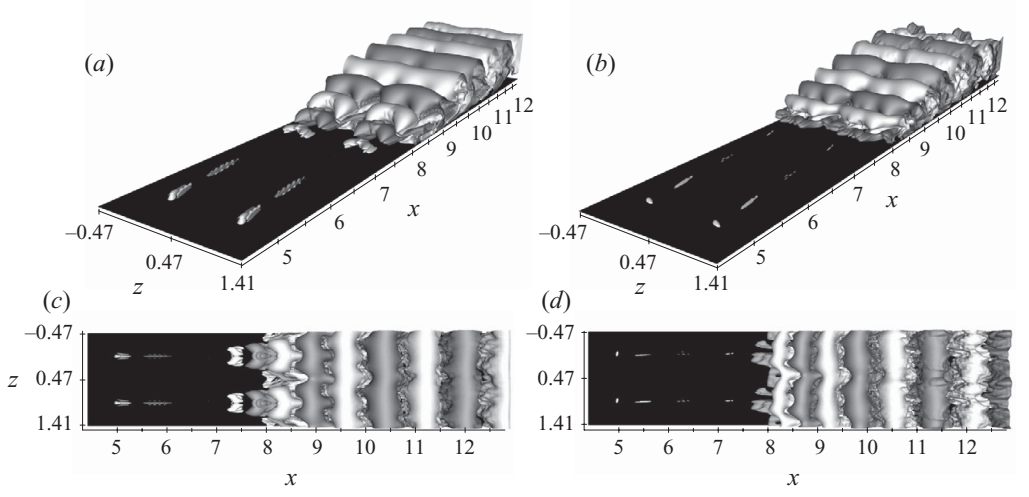


FIGURE 14. POD eigenfunctions of the wall-normal velocity (mode 1). (*a*, *c*) Case *PV*-A and (*b*, *d*) case *PA*-A. Iso-contours of $|v| = 0.025$. Perspective view (*a*,*b*) and top view (*c*,*d*) of the region $4.4 \leqslant x \leqslant 12.8$, $-0.47 \leqslant z \leqslant 1.41$.

forcing with jets through localized holes is indeed important, and this finding may have significant implications for our understanding of pulsed VGJ control.

5.1.2. *Proper orthogonal decomposition*

In this section, proper orthogonal decomposition (POD, Berkooz, Holmes & Lumley 1993) is used in an attempt to identify the dominant coherent structures present in our simulations. POD provides orthogonal basis functions (modes) which are optimized with respect to the energy content of the flow field, i.e. the largest fraction of the total kinetic energy is obtained with the least number of modes.

In the following, the 'most energetic' POD eigenfunctions of the wall-normal velocity and their respective time coefficients are presented. Figure 14 shows a side-by-side comparison of POD mode 1 for cases *PV*-A (*a*,*c*) and *PA*-A (*b*,*d*). These 'eigenfunctions' represent the most energetic *unsteady* disturbances in the flow (mode 0, which contains significantly more energy, corresponds to the mean flow). Plotted in figure 14 are iso-surfaces of the wall-normal velocity component, $|v| = 0.025$, in a perspective view and in a top view towards the surface. For illustration purposes, the

https://doi.org/10.1017/jfm.2011.34 Published online by Cambridge University Press

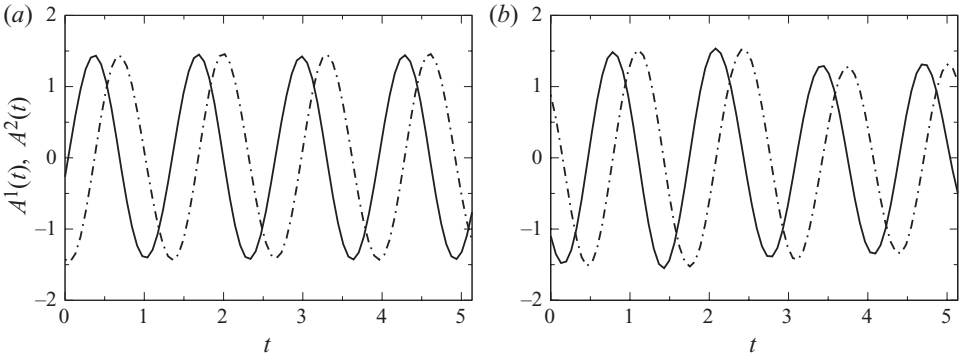


FIGURE 15. POD time functions associated with mode 1 (—) and mode 2 (— · —). (*a*) Case *PV*-A and (*b*) case *PV*-A.

spanwise domain was doubled. The presented POD results provide strong evidence for the hypothesis that the most energetic structures are predominantly *two-dimensional* in nature. In other words, the most dominant structures, in both cases, exhibit a strong spanwise coherence. This of course was not expected, as the forcing was by pulsed jets through holes, and the effectiveness of VGJs was suggested by previous studies (see Bons *et al.* 2001) to be due to the generation of longitudinal vortices.

The time-dependent POD coefficients associated with mode 1 and mode 2, $A^1(t)$ and $A^2(t)$, are given in figure 15. The phase shift in these coefficients clearly indicates that these modes form pairs which physically represent structures travelling in the downstream direction ('waves'). Furthermore, the time signals in both cases have the dominant frequency of $f \approx 0.77$, indicating that the spanwise coherent structures are synchronized with the forcing. This observation corroborates the conjecture that the pulsed VGJs, despite the inherent three-dimensionality associated with the forcing through localized holes, are indeed responsible for the generation of these large-scale spanwise structures.

5.1.3. *Generation of spanwise coherent structures by pulsed VGJs*

The answer to the question of how the observed 2D coherent structures can be generated by the pulsed VGJ injection is related to the hydrodynamic instability mechanisms that are associated with the separated boundary layer. As a result of the APG in the streamwise direction, an inflection point develops in the velocity profile, and as a result of which, the flow becomes inviscidly unstable (Kelvin–Helmholtz instability). This hydrodynamic instability leads to the growth of disturbance waves. The amplification rates increase as the inflection point in the velocity profile moves farther and farther away from the wall, and they eventually reach very large values in the separated region. It is well known from linear stability theory (LST) that inflectional velocity profiles (separated boundary layers, free shear layers, etc.) are initially most unstable with respect to two-dimensional disturbances. Consequently, upon reaching large (nonlinear) amplitudes, the disturbance waves manifest themselves as 'visible' spanwise vortices ('rollers'), whose coherence remains strong well into the fully turbulent regime (as seen from the POD modes discussed above).

In spite of the three-dimensionality associated with the forcing through localized holes, a two-dimensional disturbance component is always introduced as part of the actuation (as long as the jets are employed 'in phase' in the spanwise direction). The

https://doi.org/10.1017/jfm.2011.34 Published online by Cambridge University Press

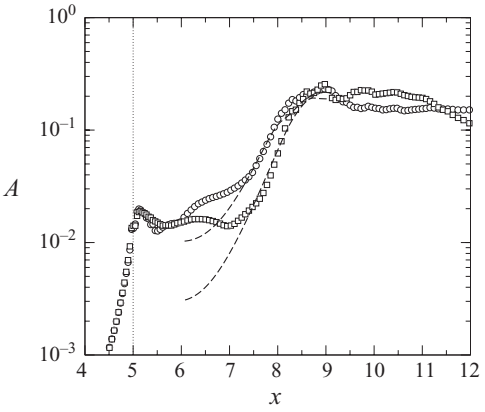


FIGURE 16. Downstream development of the Fourier amplitude for the disturbance velocity u' (maxima over y) of the fundamental frequency $f = 0.77$, the dashed line indicating the jet location: (○) vertical injection, case PV-A; (●) angled injection, case PA-A and (— — —) linear stability theory (LST).

downstream development of the two-dimensional disturbances that are introduced in this manner is illustrated in figure 16. For both vertical and angled jet injection, the maximum amplitude values (maxima over y) of the disturbance velocity u' for the fundamental frequency $f = 0.77$ as obtained from DNS are shown and compared with the results from LST. The stability analysis was performed for the streamwise velocity profiles of the time- and spanwise-averaged flow fields by assuming disturbances of the form

$$v = \tilde{v}(y)\mathrm{e}^{\mathrm{i}(\alpha x - \omega t)}, \tag{5.1}$$

and solving the well-known Orr–Sommerfeld equation

$$\left\{\left(\frac{\mathrm{d}^2}{\mathrm{d}y^2} - \alpha^2\right)^2 - \mathrm{i}\alpha Re\left[(U-c)\left(\frac{\mathrm{d}^2}{\mathrm{d}y^2} - \alpha^2\right) - \frac{\mathrm{d}^2 U}{\mathrm{d}y^2}\right]\right\}\tilde{v} = 0, \tag{5.2}$$

together with homogeneous boundary conditions, $\tilde{v} = \mathrm{d}\tilde{v}/\mathrm{d}y = 0$ at $y = 0$ and in the free stream. Equation (5.2) represents an eigenvalue problem which is solved for the wall-normal velocity distribution, $\tilde{v} = \tilde{v}(y)$, and $\alpha = 2\pi/\lambda$ (wavenumber of a travelling wave with wavelength λ). In the solution strategy we adopt the spatial mode, i.e. whereas $\tilde{v}$ and α are complex quantities, the frequency, $\omega = 2\pi f$, is a real quantity. The flow is convectively stable for $\alpha_i > 0$ (exponential decay) or unstable for $\alpha_i < 0$ (exponential growth). The amplification curves plotted in figure 16 are obtained by integrating α_i over the downstream distance:

$$A(x) = A_0(x_0)\exp\left\{-\int_{x_0}^{x} \alpha_i \mathrm{d}x'\right\}, \tag{5.3}$$

where the start of integration is $x = x_0$, and the amplitude at that location A_0 can be chosen arbitrarily. Although linear theory is based on the parallel flow assumption, it has been shown to be a reliable tool for predicting disturbance growth especially in the upstream part of LSBs (Marxen, Rist & Wagner 2004).

The amplitude growth of the 2D disturbances in figure 16 is approximately exponential (linear in the log-plot) and the good agreement between DNS and LST provides strong support for the hypothesis that linear instability mechanisms are

https://doi.org/10.1017/jfm.2011.34 Published online by Cambridge University Press

	PV-A	*PV*-B	*PV*-C	*PV*-D	*PV*-E
f	0.77	0.385	0.1925	1.54	3.08
l_R	1.71	2.06	2.26	3.82	4.55

TABLE 2. Values of the fundamental frequency, f, and the mean reattachment length, l_R, for the 3D cases presented in § 5.2.

present, and that these instability mechanisms are exploited when pulsed VGJs are employed with the 'proper' frequencies.

In a related study by Gross, Balzer & Fasel (2008) and Gross & Fasel (2010*b*) it was shown that the amplitude of the two-dimensional disturbance component can be increased by reducing the VGJ hole spacing which results in an even more efficient flow control (i.e. less C_μ) and was also found to delay transition. Conversely, increasing the hole spacing reduces the 2D disturbance amplitude but was shown to still be effective for hole spacings up to $20D$.

5.2. *Effect of the pulsing frequency*

In an effort to further corroborate the conjecture that the effectiveness of pulsed VGJs may be directly linked to a linear 2D hydrodynamic instability mechanism of the separated 'base flow', the influence of the pulsing frequency on the control effectiveness was investigated and discussed below in more detail.

5.2.1. *Three-dimensional simulations*

Since it appeared as though the relevant physical mechanisms for pulsed, angled injection were very similar to those for pulsed, vertical injection, all the simulations presented in the following were performed with pulsed, *vertical* VGJs only. In addition to case *PV*-A, four cases are considered, with forcing at various sub-harmonic as well as higher harmonic frequencies (with respect to the 'fundamental' frequency $f = 0.77$).

An overview of these simulations is given in table 2. Also listed in table 2 are the mean reattachment lengths (l_R) associated with the separation in each of the five cases. Considering l_R as a means to assess the effectiveness of a control, the 'low-frequency' cases *PV*-B and *PV*-C yield a control effectiveness that is comparable to case *PV*-A, whereas the 'high-frequency' cases *PV*-D and *PV*-E yield significantly lower effectiveness. This observation is consistent with the results presented in figure 17, where the displacement thickness (a) is plotted together with the wall-pressure distribution (b). Both graphs confirm that the VGJ effectiveness deteriorates rapidly as the forcing frequency is increased, as evidenced by the increase in separation bubble height as well as by the emerging pressure plateaus in the C_p-distributions of the 'high-frequency' cases. The cause for this behaviour is likely related to the nature of the pulsed forcing: in addition to the 'nominal' forcing frequency (i.e. $f = 0.77$ for case *PV*-A, $f = 0.385$ for case *PV*-B, etc.), a number of higher harmonics are introduced into the flow as a result of the pulsed forcing. Consequently, the flow can 'pick' the most unstable instability modes from a relatively broad spectrum. However, since this spectrum is limited to frequencies equal to and higher than the 'nominal' pulsing frequency, hydrodynamic instability mechanisms can only be exploited if the VGJs are employed at or below the frequencies to which the flow is naturally unstable.

In experiments such an optimal frequency can often not be observed. In fact, for the considered range of frequencies, the study of Bons *et al.* (2002) indicates nearly

https://doi.org/10.1017/jfm.2011.34 Published online by Cambridge University Press

	2D-A	2D-B	2D-C	2D-D	2D-E
f	0.77	0.385	0.1925	1.54	3.08
l_R	1.63	2.5	2.75	3.86	3.52

TABLE 3. Values of the fundamental frequency, f, and the mean reattachment length, l_R, for the 2D cases presented in § 5.2.

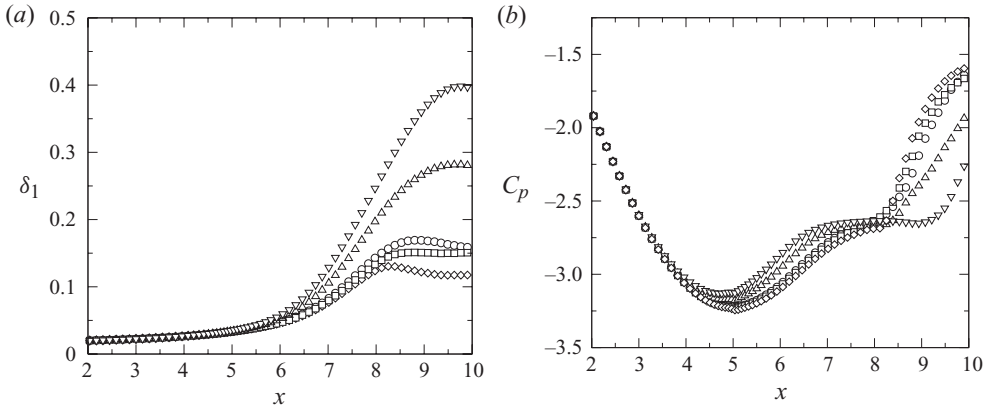


FIGURE 17. Effect of the pulsing frequency on the separation behaviour. (*a*) Time- and spanwise-averaged displacement thickness and (*b*) time- and spanwise-averaged wall-pressure coefficient. (◇) Case *PV*-A; (□) case *PV*-B; (○) case *PV*-C; (△) case *PV*-D and (▽) case *PV*-E.

equal effectiveness. However, the effectiveness was based on an integrated wake loss coefficient and not on a local parameter such as the separation length.

5.2.2. *Two-dimensional reference simulations*

For each of the 3D simulations discussed above, corresponding 2D simulations were performed in such a way as to allow for a direct comparison of the results (see table 3).

In the 2D simulations, perturbations are introduced by means of pulsed blowing through a slot, which has the same width as the diameter of the VGJ holes in the 3D simulations. The amplitude of the actuation, $B = 0.288$, was adjusted such that the momentum coefficient was the same as in the VGJ investigations.

Typical results from the 2D simulations (case 2D-A) are presented in figure 18. Shown are the instantaneous grey-scale contours of the spanwise vorticity component as well as instantaneous streamlines. As expected, highly energetic spanwise vortices can be seen to form as a result of the forcing, and these structures remain embedded in the boundary layer well downstream of reattachment (as observed with the spanwise coherent structures in case *PV*-A, for example). Due to the fact that the simulation was 2D, all 3D effects were excluded, and thus the flow cannot transition.

A comparison of the mean reattachment lengths obtained from the 2D and the 3D simulations is presented in figure 19. Of particular importance in figure 19 is the observation that, of all the cases considered (2D and 3D), the shortest separation bubble is obtained in case 2D-A ($f = 0.77$). Therefore, the 2D simulations seem to indicate that spanwise vortices ('rollers'), in theory, can provide more exchange of momentum (and hence a more effective control mechanism) than 3D mechanisms

https://doi.org/10.1017/jfm.2011.34 Published online by Cambridge University Press

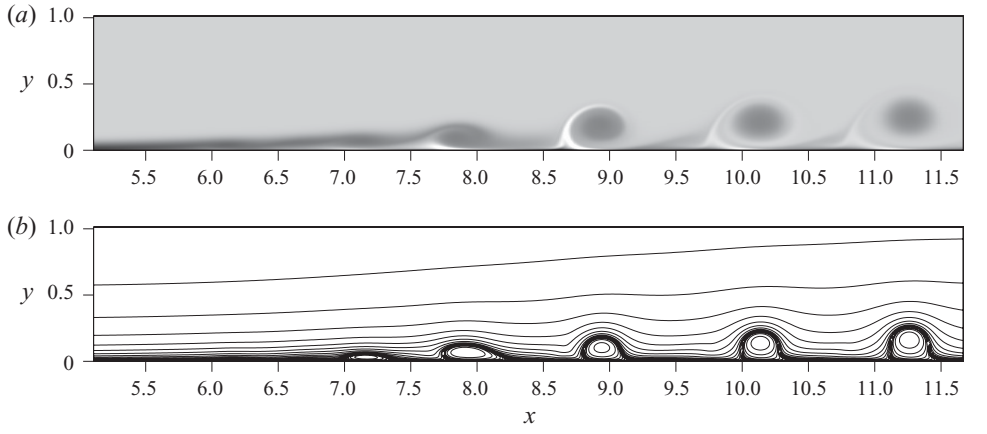


FIGURE 18. Typical results from the 2D simulation with $f = 0.77$. (*a*) Instantaneous grey-scale contours. (*b*) Instantaneous streamlines (plotted are equidistant contours of $\ln(|10^5 \times \psi| + 1)$).

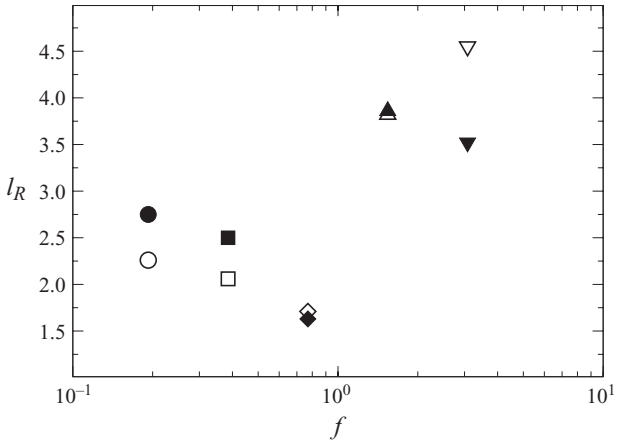


FIGURE 19. Comparison of the mean reattachment lengths for the 2D and 3D simulations. (◇) Case *PV*-A; (□) case *PV*-B; (○) case *PV*-C; (△) case *PV*-D and (▽) case *PV*-E. (◆) Case 2D-A; (■) case 2D-B; (●) case 2D-C; (▲) case 2D-D and (▼) case 2D-E.

and/or the 'turbulent mixing' associated with transitioning of the flow. However, it is in no way implied that 3D instability mechanisms are not important or that the present 2D simulations are indeed representative of what would be observed in technical applications, where highly energetic, 'laminar' spanwise vortices become susceptible to 3D secondary instabilities, which 'drain' energy from the 2D structures, thus weakening their strength. Nevertheless, the present 2D simulations serve the purpose of unequivocally establishing the importance of 2D instability modes resulting from linear hydrodynamic instability mechanisms in the context of separation control. In fact, since three-dimensional flow structures and the breakdown to turbulence are eliminated as potential flow control mechanisms, the 2D simulations lend further support to the hypothesis that spanwise vortices, whether 'laminar' or 'spanwise coherent', play an important role in controlling flow separation. Furthermore, there seems to be a direct link between the 'energy content' of the most-amplified 2D instability modes and the performance/effectiveness of the actuation. This conclusion

https://doi.org/10.1017/jfm.2011.34 Published online by Cambridge University Press

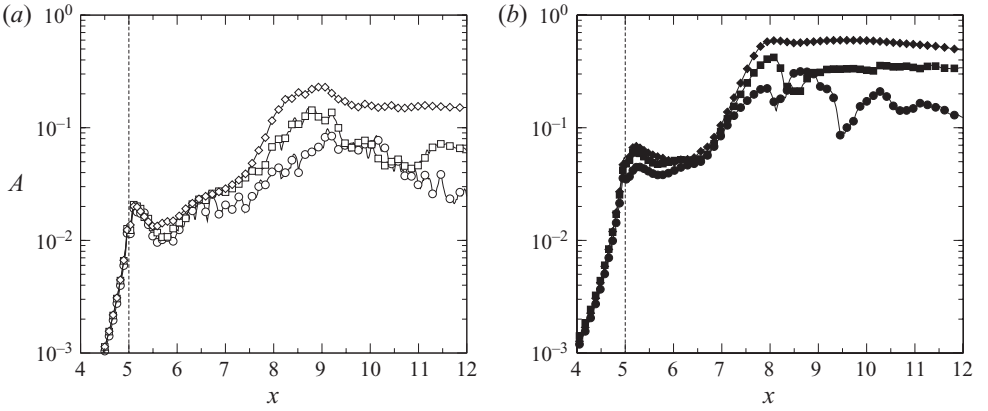


FIGURE 20. Downstream development of the Fourier amplitude for the disturbance velocity u' (max. over y) of the most-amplified frequency ($f = 0.77$). (a) 3D simulations and (b) 2D simulations. (◇) Case PV-A; (□) case PV-B; (○) case PV-C; (◆) case 2D-A; (■) case 2D-B and (●) case 2D-C.

is corroborated by the Fourier-amplitude distributions presented in figure 20. Shown is a side-by-side comparison of results obtained from the 3D simulations (a) and from the 2D simulations (b). This comparison confirms that the overall effectiveness of the forcing is reflected in the saturation amplitude of the most amplified 2D instability mode.

6. Conclusions

In this paper, laminar boundary-layer separation and its control were investigated by direct numerical simulations. A laminar boundary layer on a flat plate was subjected to the same streamwise pressure gradient as measured in a low-pressure turbine blade cascade, and the resulting flow separation was controlled by means of vortex generator jets (VGJs).

In agreement with previously published work, it was found that pulsed blowing is indeed significantly more effective in reducing laminar boundary-layer separation than steady blowing when the same momentum coefficient was used for the actuation. In contrast to suggestions in the literature, the present investigations demonstrate that the relevant physical mechanisms associated with pulsed VGJs are entirely different from those associated with steady VGJs. Whereas steady forcing generates longitudinal vortices which aid in the entrainment of free-stream momentum, the relevant physical mechanisms associated with pulsed forcing were identified as being related to the formation of *spanwise* coherent structures that develop as a result of linear hydrodynamic instability mechanisms of the separated shear layer. An indication for the relevance of this physical mechanism is that the simulations for pulsed, angled jet injection and pulsed, vertical injection yielded very similar results. The conjecture that linear instability mechanisms are primarily responsible for the development of predominantly two-dimensional coherent structures is corroborated by the observation that the pulsing frequency is an important control parameter. For pulsed blowing to be effective and efficient, the jets have to be employed within the range of naturally unstable frequencies. As a consequence of our investigations, we believe that for *effective* and *efficient* control of separation it is crucial that

https://doi.org/10.1017/jfm.2011.34 Published online by Cambridge University Press

[H]

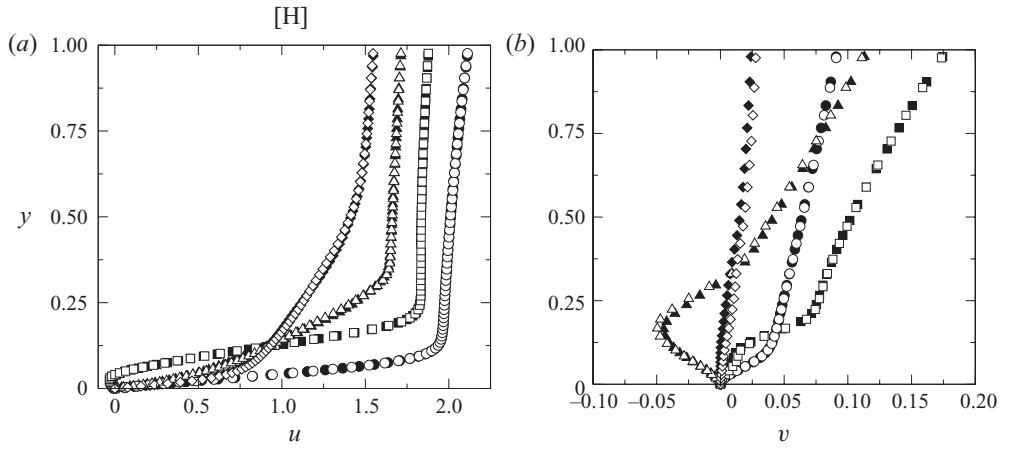


FIGURE 21. Selected time- and spanwise-averaged velocity profiles for the 'normal' grid (case *PV*-A) and the 'fine' grid (*PV*-A_2). (*a*) u and (*b*) v. Open symbols: 'normal' grid; filled symbols: 'fine' grid. (○/●) $x = 6$; (□/■) $x = 8$; (△/▲) $x = 9$ and (◇/◆) $x = 12$.

hydrodynamic stability mechanisms are exploited. These findings have a much broader applicability than just the control of flow separation for low-pressure turbine blades. Rather, they directly apply to other flows such as on aerofoils and using control actuators other than pulsed jets (see Gross & Fasel 2010*a*, for example). Exploiting hydrodynamic instability mechanisms is clearly the key to both effective and efficient flow control of separation.

The present work has been supported by the Air Force Office of Scientific Research grants F49620-02-1-0122 and FA9550-05-1-0166 with Dr Thomas Beutner and Lt Col. Rhett Jefferies serving as program managers. Computer time was provided by the Army High Performance Computing Research Center (AHPCRC), the Engineer Research and Development Center (ERDC) and the Arctic Region Supercomputing Center (ARSC).

Supplementary movies are available at journals.cambridge.org/flm.

Appendix A. Grid study

With the exception of cases *UNF*, *SV*-A and *SA*-A, all the simulations presented in this paper were performed with a computational grid (see figure 23) that consists of approximately 31 million points (1025 points in the x-direction, 193 points in the y-direction and 160 collocation points in the z-direction). In order to establish that this 'baseline' grid is sufficiently fine to properly resolve all relevant scales present in the flow, one simulation was performed with an extremely 'fine' grid, which consisted of approximately 164 million points (1601 points in the x-direction, 321 points in the y-direction and 320 collocation points in the z-direction). In this simulation, the forcing parameters are the same as in case *PV*-A – hence the notation *PV*-A_2. In figures 21 and 22, selected flow quantities are compared for the 'normal' grid and the 'fine' grid, and the results indicate that the grid refinement changes the solution only insignificantly.

https://doi.org/10.1017/jfm.2011.34 Published online by Cambridge University Press

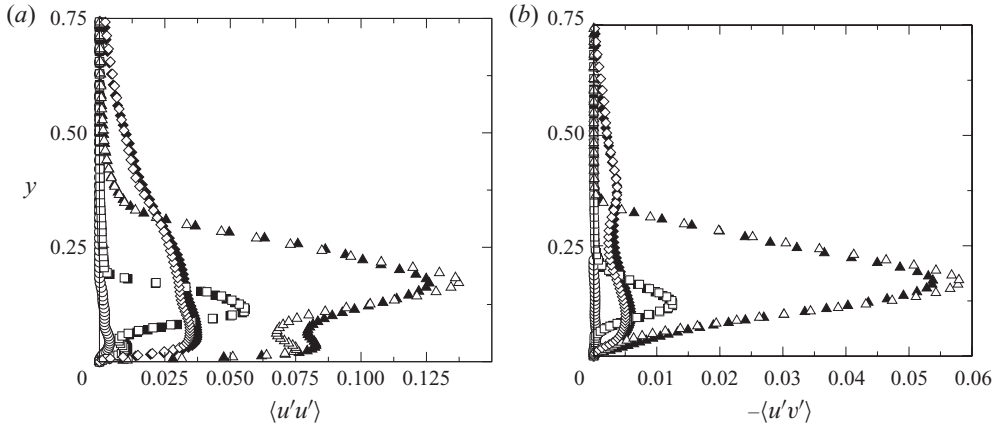


FIGURE 22. Selected spanwise-averaged Reynolds stresses for the 'normal' grid (case *PV*-A) and the 'fine' grid (case *PV*-A_2). (*a*) $\langle u'u' \rangle$ and (*b*) $-\langle u'v' \rangle$. Open symbols: 'normal' grid; filled symbols: 'fine' grid. (○/●) $x = 6$; (□/■) $x = 8$; (△/▲) $x = 9$ and (◇/◆) $x = 12$.

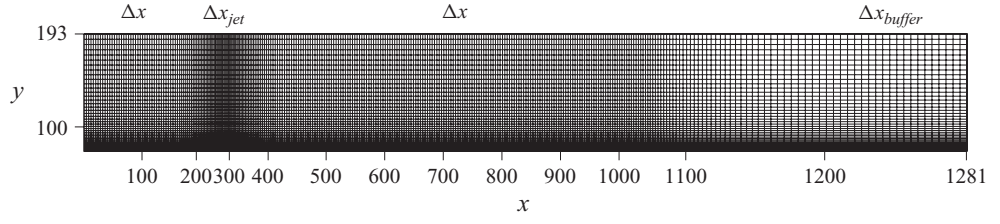


FIGURE 23. Schematic of a typical DNS grid. Only every fourth point is shown in both x and y.

Case	I, J	$(2K+1), \mathscr{K}$	Δx	Δx_{jet}	Δx_{buffer}	Δy_{wall}	Δz	Δt
UNF	801, 129	49, 80	0.025	N/A	0.025	2.5×10^{-3}	0.012	4.4×10^{-3}
TRIP	1025, 193	97, 160	0.0125	6.25×10^{-3}	0.0375	1.6×10^{-3}	0.006	1.7×10^{-3}
SV-A	1281, 193	97, 160	0.0125	6.25×10^{-3}	0.0375	1.6×10^{-3}	0.006	1.7×10^{-3}
SA-A	1281, 193	97, 160	0.0125	6.25×10^{-3}	0.0375	1.6×10^{-3}	0.006	1.7×10^{-3}
PV-A	1025, 193	97, 160	0.0125	6.25×10^{-3}	0.0375	1.6×10^{-3}	0.006	1.7×10^{-3}
PV-A_2	1601, 321	193, 320	0.0078	3.91×10^{-3}	0.02	9.8×10^{-4}	0.003	1×10^{-3}
PA-A	1025, 193	97, 160	0.0125	6.25×10^{-3}	0.0375	1.6×10^{-3}	0.006	1.7×10^{-3}
PV-B	1025, 193	97, 160	0.0125	6.25×10^{-3}	0.0375	1.6×10^{-3}	0.006	1.7×10^{-3}
PV-C	1025, 193	97, 160	0.0125	6.25×10^{-3}	0.0375	1.6×10^{-3}	0.006	1.7×10^{-3}
PV-D	1025, 193	97, 160	0.0125	6.25×10^{-3}	0.0375	1.6×10^{-3}	0.006	1.7×10^{-3}
PV-E	1025, 193	97, 160	0.0125	6.25×10^{-3}	0.0375	1.6×10^{-3}	0.006	1.7×10^{-3}
2D-A	1025, 193	N/A	0.0125	6.25×10^{-3}	0.0375	1.6×10^{-3}	N/A	1.7×10^{-3}
2D-B	1025, 193	N/A	0.0125	6.25×10^{-3}	0.0375	1.6×10^{-3}	N/A	1.7×10^{-3}
2D-C	1025, 193	N/A	0.0125	6.25×10^{-3}	0.0375	1.6×10^{-3}	N/A	1.7×10^{-3}
2D-D	1025, 193	N/A	0.0125	6.25×10^{-3}	0.0375	1.6×10^{-3}	N/A	1.7×10^{-3}
2D-E	1025, 193	N/A	0.0125	6.25×10^{-3}	0.0375	1.6×10^{-3}	N/A	1.7×10^{-3}

TABLE 4. Computational parameters.

https://doi.org/10.1017/jfm.2011.34 Published online by Cambridge University Press

Case	x_{jet}	$\mathscr{D}$	φ	θ	B	C_μ	f	τ
SV-A	5	0.1	90°	0°	0.316	1.2×10^{-4}	N/A	N/A
SA-A	5	0.1	30°	−90°	0.316	1.2×10^{-4}	N/A	N/A
PV-A	5	0.1	90°	0°	1	1.2×10^{-4}	0.77	10 %
PV-A_2	5	0.1	90°	0°	1	1.2×10^{-4}	0.77	10 %
PA-A	5	0.1	30°	−90°	1	1.2×10^{-4}	0.77	10 %
PV-B	5	0.1	90°	0°	1	1.2×10^{-4}	0.385	10 %
PV-C	5	0.1	90°	0°	1	1.2×10^{-4}	0.1925	10 %
PV-D	5	0.1	90°	0°	1	1.2×10^{-4}	1.54	10 %
PV-E	5	0.1	90°	0°	1	1.2×10^{-4}	3.08	10 %
2D-A	5	0.1 (⋆)	N/A	N/A	0.288	1.2×10^{-4}	0.77	10 %
2D-B	5	0.1 (⋆)	N/A	N/A	0.288	1.2×10^{-4}	0.385	10 %
2D-C	5	0.1 (⋆)	N/A	N/A	0.288	1.2×10^{-4}	0.1925	10 %
2D-D	5	0.1 (⋆)	N/A	N/A	0.288	1.2×10^{-4}	1.54	10 %
2D-E	5	0.1 (⋆)	N/A	N/A	0.288	1.2×10^{-4}	3.08	10 %

TABLE 5. VGJ control parameters. (⋆) Values represent the slot width.

Appendix B. Computational parameters

The relevant computational parameters are summarized in tables 4 and 5.

REFERENCES

ALAM, M. & SANDHAM, N. D. 2000 Direct numerical simulation of 'short' laminar separation bubbles with turbulent reattachment. *J. Fluid Mech.* **403**, 223–250.

BAKE, S., MEYER, D. & RIST, U. 2002 Turbulence mechanism in Klebanoff transition: a quantitative comparison of experiment and direct numerical simulation. *J. Fluid Mech.* **459**, 217–243.

BALZER, W. & FASEL, H. F. 2010 Numerical investigation of the effect of free-stream turbulence on laminar boundary-layer separation. *AIAA Paper* 2010-4600.

BERKOOZ, G., HOLMES, P. & LUMLEY, J. L. 1993 The proper orthogonal decomposition in the analysis of turbulent flows. *Annu. Rev. Fluid Mech.* **25**, 539–575.

BLOXHAM, M., REIMANN, D., CRAPO, K., PLUIM, J. & BONS, J. 2007 Synchronizing separation flow control with unsteady wakes in a low-pressure turbine cascade. In *IGTI Conference, International Gas Turbine Inst. Paper GT2007-27529*, Montreal, Canada.

BONS, J. P., HANSEN, L. C., CLARK, J. P., KOCH, P. J. & SONDERGAARD, R. 2005 Designing low-pressure turbine blades with integrated flow control. In *Proceedings of GT2005, ASME Turbo Expo 2005: Power for Land, Sea, and Air*, Reno-Tahoe, NV.

BONS, J. P., SONDERGAARD, R. & RIVIR, R. B. 2001 Turbine separation control using pulsed vortex generator jets. *ASME J. Turbomach.* **123**, 198–206.

BONS, J. P., SONDERGAARD, R. & RIVIR, R. B. 2002 The fluid dynamics of LPT blade separation control using pulsed jets. *ASME J. Turbomach.* **124**, 77–85.

DAVIES, C. & CARPENTER, P. W. 2001 A novel velocity–vorticity formulation of the Navier–Stokes equations with applications to boundary layer disturbance evolution. *J. Comput. Phys.* **172**, 119–165.

FASEL, H. F. 1976 Investigation of the stability of boundary layers by a finite-difference model of the Navier–Stokes equations. *J. Fluid Mech.* **78** (2), 355–383.

FERZIGER, J. H. 1998 *Numerical Methods for Engineering Application*, 2nd edn. Wiley.

GASTER, M. 1966 The structure and behaviour of laminar separation bubbles. In *AGARD CP 4*, pp. 813–854.

GIER, J., FRANKE, M., HÜBNER, N. & SCHRÖDER, T. 2008 Designing LP turbines for optimized airfoil lift. In *Proceedings of GT2008, ASME Turbo Expo 2008: Power for Land, Sea, and Air*, Berlin, Germany.

https://doi.org/10.1017/jfm.2011.34 Published online by Cambridge University Press

Gross, A., Balzer, W. & Fasel, H. F. 2008 Active separation control for lifting surfaces at low-Reynolds number operating conditions. In *HPCMP-UGC '08: Proceedings of the 2008 DoD High Performance Computing Modernization Program Users Group Conference, Washington, DC, USA*, pp. 9–17. IEEE Computer Society.

Gross, A. & Fasel, H. F. 2010*a* Active flow control for NACA 6-series airfoil at $Re = 64{,}200$. *AIAA J.* **48** (9), 1889–1902.

Gross, A. & Fasel, H. F. 2010*b* Numerical simulation of low-pressure turbine blade separation control. *AIAA J.* **48** (8), 1582–1601.

Gruber, K. 1987 Numerische Untersuchungen zum Problem der Grenzschichtablösung. PhD thesis, Universität Stuttgart.

Haidari, A. H. & Smith, C. R. 1994 The generation and regeneration of single hairpin vortices. *J. Fluid Mech.* **277**, 135–161.

Gad-el Hak, M., Pollard, A. & Bonnet, J.-P. (Ed.) 1998 *Flow Control: Fundamentals and Practices*. Springer.

Horton, H. P. 1968 Laminar separation in two and three-dimensional incompressible flow. PhD thesis, University of London.

Huerre, P. & Monkewitz, P. A. 1990 Local and global instabilities in spatially developing flows. *Annu. Rev. Fluid Mech.* **22**, 473–537.

Jeong, J. & Hussain, F. 1995 On the identification of a vortex. *J. Fluid Mech.* **285**, 69–94.

Johari, H. & McManus, K. 1997 Visualization of pulsed vortex generator jets for active control of boundary layer separation. *AIAA Paper* 97-2021.

Johari, H. & Rixon, G. S. 2003 Effects of pulsing on a vortex generator jet. *AIAA J.* **41** (12), 2309–2315.

Jones, L. E. & Sandberg, R. D., Sandham N. D. 2008 Direct numerical simulations of forced and unforced separation bubbles on an airfoil at incidence. *J. Fluid Mech.* **602**, 175–207.

Lele, S. K. 1992 Compact finite difference schemes with spectral-like resolution. *J. Comput. Phys.* **103**, 16–42.

Liu, J. T. C. 1989 Coherent structures in transitional and turbulent free shear flows. *Annu. Rev. Fluid Mech.* **21**, 285–315.

Marxen, O., Lang, M., Rist, U., Levin, O. & Henningson, D. S. 2009 Mechanisms for spatial steady three-dimensional disturbance growth in a non-parallel and separating boundary layer. *J. Fluid Mech.* **634**, 165–189.

Marxen, O. & Rist, U. 2010 Mean flow deformation in a laminar separation bubble: separation and stability characteristics. *J. Fluid Mech.* **660**, 37–54.

Marxen, O., Rist, U. & Wagner, S. 2004 Effect of spanwise-modulated disturbances on transition in a separated boundary layer. *AIAA J.* **42**, 937–944.

McManus, K., Joshi, P., Legner, H. & Davis, S. 1995 Active control of aerodynamic stall using pulsed jet actuators. *AIAA Paper* 95-2187.

McManus, K., Legner, H. & Davis, S. 1994 Pulsed vortex generator jets for active control of separation. *AIAA Paper* 94-2218.

Meitz, H. & Fasel, H. F. 2000 A compact-difference scheme for the Navier–Stokes equations in vorticity–velocity formulation. *J. Comput. Phys.* **157**, 371–403.

Morkovin, M. V. 1969 The many faces of transition. In *Viscous Drag Reduction* (ed. C. S. Wells). Plenum.

Orszag, S. A. 1971 Numerical simulation of incompressible flows within simple boundaries: galerkin (spectral) representations. *Stud. Appl. Maths* **50**, 293–327.

Pauley, L. L. 1994 Response of two-dimensional separation to three-dimensional disturbances. *J. Fluids Engng* **116**, 433–438.

Pauley, L. L., Moin, P. & Reynolds, W. C. 1990 The structure of two-dimensional separation. *J. Fluid Mech.* **220**, 397–411.

Postl, D. 2005 Numerical investigation of laminar separation control using vortex generator jets. PhD thesis, University of Arizona.

Postl, D. & Fasel, H. F. 2006 Direct numerical simulation of turbulent flow separation from a wall-mounted hump. *AIAA J.* **44** (2), 263–272.

Ripley, M. D. & Pauley, L. L. 1993 The unsteady structure of two–dimensional steady laminar separation. *Phys. Fluids* **5** (12), 3099–3106.

https://doi.org/10.1017/jfm.2011.34 Published online by Cambridge University Press

Rist, U. & Fasel, H. F. 1995 Direct numerical simulation of controlled transition in a flat-plate boundary layer. *J. Fluid Mech.* **298**, 211–248.

Rist, U. & Maucher, U. 1994 Direct numerical simulations of 2D and 3D instability waves in a laminar separation bubble. In *Proceedings of the AGARD Symposium on Application of Direct and Large Eddy Simulation to Transition and Turbulence, AGARD CP 551*, Chania, Crete, Greece.

Schmid, P. J. & Henningson, D. S. 2001 *Stability and Transition in Shear Flows*. Springer.

Sondergaard, R., Bons, J. P. & Rivir, R. B. 2002 Control of low-pressure turbine separation using vortex generator jets. *J. Propul. Power* **18**, 889–895.

Spalart, P. R. & Strelets, M. K. 2000 Mechanisms of transition and heat transfer in a separation bubble. *J. Fluid Mech.* **403**, 329–349.

Watmuff, J. H. 1999 Evolution of a wave packet into vortex loops in a laminar separation bubble. *J. Fluid Mech.* **397**, 119–169.

https://doi.org/10.1017/jfm.2011.34 Published online by Cambridge University Press